ROYAL SOCIETY OF CHEMISTRY

PAPER

Check for updates

Fluorane sensitive supercapacitive microcrystalline MoO₃: dual application in energy storage and HF detection†

Love Bansal,[a] Tanushree Ghosh,[a] Suchita Kandpal,[ab] Chanchal Rani,‡[a] Bhumika Sahu,[a] Deb Kumar Rath,[a] Christoph Wesemann,[cd] Sandeep Chhoker,[e] Nadja C. Bigall [ID] *[cd] and Rajesh Kumar [ID] *[af]

Exploring materials and device paradigms for multifunctional electrochemical applications such as supercapacitors and sensing makes materials more suitable for real-life applications. In this study, microcrystalline MoO₃ powder has been synthesized using a simple sol–gel method, and its suitability for energy storage devices and HF sensing performance has been studied. The MoO₃ microcrystallites, well-characterized using electron microscopy, X-ray diffraction, and Raman spectroscopy, have been tested for HF sensitivity on a glassy carbon electrode as well as on a carbon cloth electrode. Similarly, a solid-state prototype asymmetric supercapacitor has been demonstrated that displays its charge storage capabilities. The specific capacitance of MoO₃ increases linearly with the increase of HF concentration. Additionally, the sensing performance of MoO₃ can be seen by monitoring changes in current passing through the electrode in the presence of HF. High stability with good repeatability was displayed. *In situ* Raman spectroscopy, recorded during the charging and discharging process, has been used to understand the charge storage mechanism. A high sensitivity of 6656 mF mM^{-1} g^{-1} with a low limit of detection of 1.2 μM was observed, which makes this material suitable for sensing as well as charge storage.

Introduction

Chemical waste from an industry that is illegally disposed of or improperly treated has massively contaminated the environment around such industrial facilities leading to several

[a] *Materials and Device Laboratory, Department of Physics, Indian Institute of Technology Indore, Simrol-453552, India. E-mail: rajeshkumar@iiti.ac.in*

[b] *Department of Chemical and Biomolecular Engineering, Cornell University, Ithaca, NY 14853, USA*

[c] *Institute of Physical Chemistry and Electrochemistry (PCI), Gottfried Wilhelm Leibniz University Hannover, Callinstr. 3a, D-30167 Hannover, Germany. E-mail: nadja.bigall@pci.uni-hannover.de*

[d] *Cluster of Excellence PhoenixD (Photonics, Optics and Engineering – Innovation Across Disciplines), Leibniz University Hannover, D-30167 Hannover, Germany*

[e] *Department of Physics and Material Science and Engineering, Jaypee Institute of Information Technology, Noida, 201307, India*

[f] *Centre for advanced electronics, Indian Institute of Technology Indore, Simrol-453552, India*

† Electronic supplementary information (ESI) available: A detailed description of electrochemical measurements, FESEM images, CV graph, variation of specific capacitance with current density, GCD plot, variation of peak current with HF concentration, Raman shift and after electrochemical characterization of MoO₃/GCE, CV curve, repeatability test, FESEM image of MoO₃/CC, and comparison table. See DOI: https://doi.org/10.1039/d3ma00357d

‡ Current Address: Department of Chemistry, University of Michigan, Ann Arbor, Michigan 48109, United States of America.

hazards and consequent health issues.[1,2] Therefore, the need for sensors to detect contamination, *e.g.*, in flowing waters, has risen drastically.[3–5] Hydrofluoric acid, or HF, is a commonly used material in various industries related to pharmaceuticals, herbicides, glass manufacturing, ceramics and metals (as surface treatment agents), photovoltaics, and the food industry due to its use as a reducing agent.[6] Exposure to HF even in very low concentrations can cause severe health issues such as skin damage, eye irritation, visual disturbances, *etc.*[7] Due to all the above factors, detection of HF is very crucial.[8] In recent years, many sensors have been fabricated based on calorimetry,[9] chemiluminescence,[10] fluorescence,[11] chromatography,[12] colorimetry sensors,[13] *etc.* Typically sensors have many disadvantages, such as a difficult preparation process, poor sensitivity, an unacceptable limit of detection, low reproducibility, limited storage time, *etc.*[14] To overcome the above disadvantages, electrochemical sensing methods could prove to be a better alternative due to their advantages such as high repeatability, high sensitivity, a low limit of detection, real time monitoring, easy fabrication, *etc.*[15] Moreover, electrochemical sensing based on supercapacitive behaviour is expected to have further high sensitivity and a low limit of detection as compared to electrochemical sensing using the *I–V* curve, which reads current at the voltage for various concentrations.

Electrochemical sensing using specific capacitance reads the area under the CV curve, a combination of current values for a potential range for various concentrations. Due to this property as mentioned above the area under the CV curve is more sensitive to material concentration as compared to I–V based electrochemical sensing. In other words, electrochemical response from appropriate materials in terms of area under CV while under an HF environment can be used as the experimental observable to detect HF in trace amounts as has been studied here.

The performance of an electrochemical sensor is governed mainly by the redox reactions occurring at the working electrode. The working electrode materials can be either anodic or cathodic depending upon the need for the type of sensing material, $e.g.$, H_2O_2 is an oxidizing agent, so it requires an anodic type material to be detected, whereas HF is a reducing agent, so it requires a cathodic material to be detected. Transition metal oxides (TMOs) such as NiO,[16] Co₃O₄,[17,18] WO₃,[19] ZnO,[20] MoO₃,[21] TiO₂,[18] $etc.$ have been explored for electrochemical sensing,[22] electrochromic devices,[23,24] supercapacitors[25–27] and battery performance.[28] The supercapacitor can be either an electric double-layer supercapacitor[29] (non-faradaic or EDLC) or a pseudocapacitor[30,31] (faradaic or redox active). Materials with pseudocapacitive properties can also be used as sensors, depending upon their redox activity. Another metal oxide, MoO₃, with an orthorhombic phase, has been studied over the last two decades for potential energy storage devices[32,33] (like lithium capacitors). However, the applications of MoO₃ in a device form are not yet established due to low specific capacitance and poor charging/discharging rates due to kinetic issues linked with poor electrical conductivity, structural stability during the charge–discharge process, and limited scalability in its preparation.[34,35] Additionally, MoO₃ is a cathodic pseudocapacitive material and hence can be used to detect reducing agents[36–38] like HF. Looking at this combination, being a charge storage material as well as a possible HF detector, it will be interesting to investigate the electrochemical properties of suitably designed (micro-)crystalline MoO₃ for bifunctional applications.

In this paper, an economic sol–gel technique was used to synthesize microcrystalline MoO₃ to be used as an electrode material for charge storage and HF sensing applications. Prior to this above-mentioned application, this material was characterized by scanning electron microscopy (SEM), elemental diffraction X-ray spectroscopy (EDX), transmission electron microscopy (TEM), X-ray diffraction (XRD), and Raman spectroscopy. The MoO₃ powder was deposited on a glassy carbon electrode (GCE) and carbon cloth (CC) for charge storage supercapacitive and sensing performance. When measured in the three-electrode cell, the MoO₃ deposited on the GCE shows a high sensitivity and low detection limit (LOD), and better charge storage capabilities. Electrochemical impedance spectroscopy (EIS) was employed to understand the charge storage mechanism. The chronoamperometric response of MoO₃ on CC shows high selectivity, fast response time, and high current retention. Electrochemical measurements of

different batches of MoO₃ samples show high reproducibility and repeatability. Furthermore, a prototype solid-state supercapacitor has been fabricated onto which $in situ$ Raman spectroscopy has also been carried out to understand the charge storage mechanism by recording Raman spectra during the charging and discharging processes.

Experimental details

Sample preparation

Sodium molybdate dihydrate (Na₂MoO₄·2H₂O), citric acid (C₆H₈O₇), lithium perchlorate (LiClO₄), hydrofluoric acid (HF), propylene carbonate (PC), and nitric acid (HNO₃) were procured commercially and used as received from Alfa Aesar™/ Sigma Aldrich™. Sodium molybdate dihydrate, nitric acid, and citric acid were used to synthesize molybdenum trioxide (MoO₃) powder using a sol–gel synthesis method. The precursor solution was prepared by dissolving 0.01 M (50 mg) sodium molybdate in 20 mL deionized water (DI). Furthermore, 0.016 M of HNO₃ (20 μL) was added dropwise in the precursor solution under constant stirring for over 30 min. 0.1 M of citric acid as a surfactant was added to the solution and stirred for 1 h. The resulting solution was kept in an oven at 120 °C for 6 h. The resultant precipitate from the heating process was annealed at 450 °C for 3 h under an inert atmosphere. The powder after annealing was collected for further characterization without any purification.

Device fabrication

The GCE was chosen as the working electrode to check the electrochemical performance, and CC (2×1 cm²) was chosen as the working electrode for electrochemical sensing experiments and symmetric supercapacitive device performance measurements of MoO₃. A homogeneous solution consisting of active material (MoO₃), activated charcoal, and Nafion in a mass ratio of 80 : 10 : 10 was prepared in DI. Afterward, 5 μL and 50 μL of the above homogeneous solution were drop cast on GCE (MoO₃/GCE) and CC (1×1 cm²) (MoO₃/CC), respectively and dried for 24 h in a desiccator. To prepare the liquid electrolyte less asymmetric supercapacitor device (MoO₃//AC), MoO₃/CC was chosen as the current collector, and Whitman filter paper soaked in 0.5 M LiClO₄ + 1 mM HF in propylene carbonate (PC) electrolyte was used as a separator. The wet separator was sandwiched between MoO₃/CC and wrapped by two glass slides to give stability. The edges of the device were covered by Teflon tape to ensure no exchange of oxygen ions from the atmosphere to the device.

Sample characterization

A JEOL IT 500 field emission scanning electron microscope (SEM) was used for surface morphology study. The transmission electron microscope (TEM) images were taken with a FEI Tecnai G2 F20 TMP operated using an emission field gun at 200 kV to investigate the particle morphology. The dried MoO₃ sample was collected on the surface of carbon covered copper
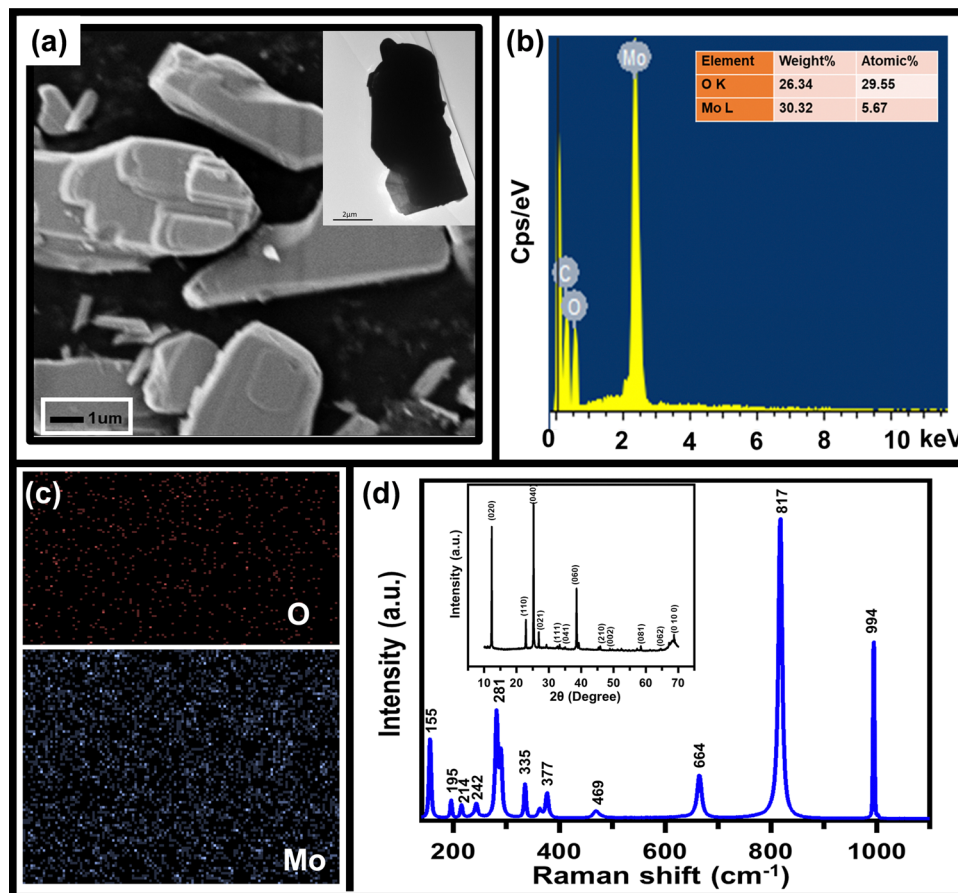
Fig. 1 Characterization of as-synthesized MoO_3 powder as seen using (a) SEM micrograph along with TEM image (inset), (b) EDX spectrum for elemental confirmation (inset: elemental composition table), (c) elemental composition, and (d) Raman spectrum and XRD pattern (inset).

grids (300 mesh) from Quantifoil by wiping the grid over the powdered sample. Energy dispersive X-ray (EDX) was applied for elemental compositional analysis. A Horiba Jobin–Yvon Raman spectrometer with a 633 nm excitation laser was used to record the Raman spectrum. A Bruker D2-Phaser diffractometer was used for X-ray diffraction (XRD) using a Cu K_α wavelength of 1.54 Å. A Metrohm-Multi Autolab M204 potentiostat was used for cyclic voltammetry, electrochemical impedance spectroscopy, galvanostatic charge discharge, and chronoamperometric response measurements using the parameters as discussed later on.

Results and discussion

As mentioned above, to achieve high electrochemical sensitivity, a porous structure is preferred.[39] Prior to being used as an electrochemical sensor and supercapacitor, the as-synthesized MoO_3 electrode was characterized using different techniques (Fig. 1) to check its surface morphology, elemental composition, phase, and purity. The SEM image (Fig. 1a) indicates high surface porosity with irregularly shaped microcrystals of MoO_3, implying more diffusion of electrolyte ions for achieving high

electrochemical performance. Uniform deposition of the cuboidal structure of MoO_3 powder of a few micrometres in size uniformly spread over the surface can be seen in the low magnification SEM image (Fig. S1, ESI†). The cuboidal geometry of MoO_3 can also be seen in the TEM image (inset, Fig. 1a). To further confirm the elemental composition of MoO_3 powder, EDX spectra were recorded (Fig. 1b). The EDX spectra confirm the presence of Mo and O atoms within the powder without any noticeable impurities. The elemental mapping of MoO_3 (Fig. 1c) indicates the uniform atomic distribution of Mo and O atoms all over the surface. To further confirm the phase of MoO_3, the Raman spectrum was recorded (Fig. 1d), which shows peaks at 155, 195, 214, 242, 281, 335, 377, 469, 664, 817, and 994 cm^{-1} indicating the orthorhombic phase of MoO_3.[40,41] The absence of other peaks in the Raman spectrum further indicates the high purity of the synthesized MoO_3 powder. To further validate the crystal phase of the sample, XRD was carried out (inset, Fig. 1d), which shows diffraction peaks at $2\theta = 12, 23, 25, 27, 29, 33, 35, 38, 46, 49, 58, 65,$ and $69°$ confirming the orthorhombic phase of MoO_3 powder (JCPDS no 050508),[42,43] making it consistent with the Raman results. Overall, the morphological, spectroscopic, and diffraction techniques confirm the synthesis of the orthorhombic phase of
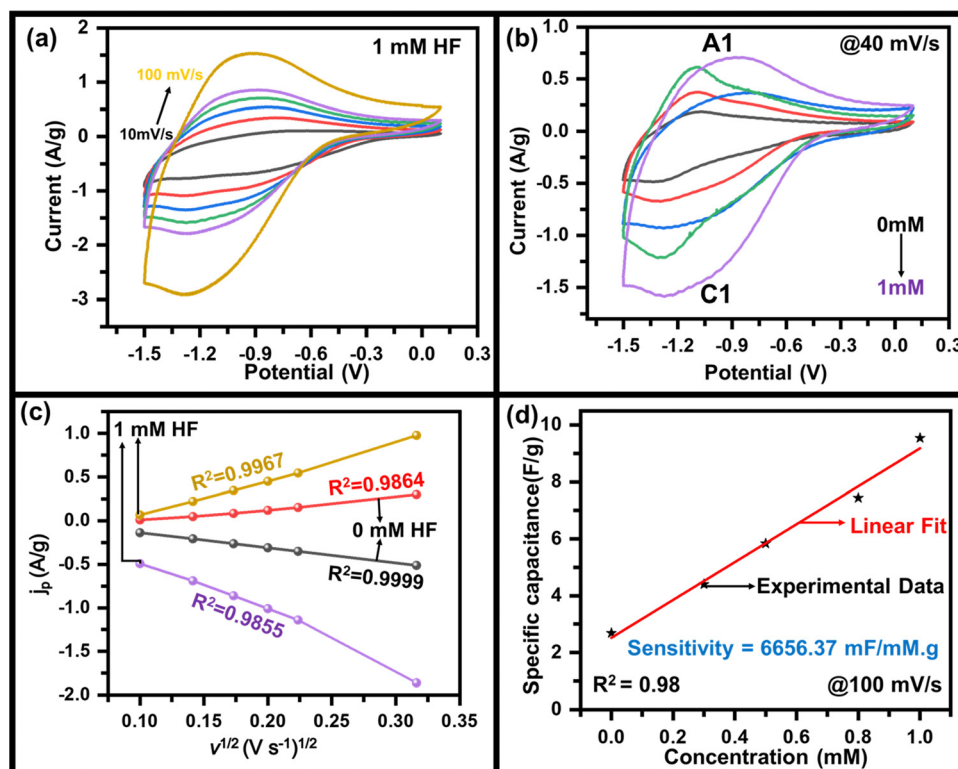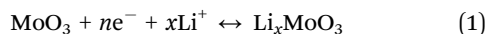
Fig. 2 CV graph of MoO$_3$ at GCE with (a) 1 mM HF, (b) 0 mM, 0.2 mM, 0.5 mM, 0.8 mM, and 1.0 mM HF in 0.5 M LiClO$_4$ in PC, (c) variation of current density (j_p) *vs.* $v^{1/2}$ graph with and without HF, and (d) variation of specific capacitance with concentration of HF including raw data and linear fit.

MoO$_3$ with porous nature as required for better electrochemical performances.

The sensing of hydrofluoric acid was carried out by three-electrode electrochemical measurements by adding a definite amount of HF to the electrolyte. The CV curves of MoO$_3$/GCE (Fig. 2a) measured in 0.5 M LiClO$_4$ with 1 mM HF in PC show a typical CV variation with varying scan rates (10 mV s^{-1} to 100 mV s^{-1}). The increase in the current density with increasing scan rate indicates the faster diffusion of electrolyte ions towards the surface at high scan rates.

The reaction governing the Li$^+$ insertion due to charging and Li$^+$ extraction during the discharge process is given by following the redox reaction eqn (1):

$$MoO_3 + ne^- + xLi^+ \leftrightarrow Li_xMoO_3 \qquad (1)$$

During the cathodic scan, MoO$_3$ is reduced to Li$_x$MoO$_3$, whereas during the anodic scan, the Li$_x$MoO$_3$ is converted back to MoO$_3$. It is crucial here to mention that the CV curve shape depends on the concentration of HF in the electrolyte, as can be seen in Fig. S2 (ESI†), which shows CV curves of MoO$_3$/GCE at various scan rates with different concentrations of HF (0 mM to 0.8 mM). The effect of HF concentration can be seen by comparing the CV graphs of MoO$_3$/GCE at various concentrations of HF (0 mM to 1 mM HF in the electrolyte) recorded at a given scan rate of 40 mV s^{-1} (Fig. 2b). The anodic and cathodic peak currents increase proportionally to the HF concentration. The cathodic peak (marked as C1) current increases with concentration and shows a linear change with HF

concentration, likely because HF is a reducing agent and can accept electrons from MoO$_3$. The CV curve also reveals that the oxidation of HF is taking place in a quasi-reversible regime for the anodic peak (marked A1) current, whereas for the cathodic peak (marked C1) current it is reversible. To further quantify the reduction of HF, peak current density (i_p) as a function of scan rate ($\nu^{1/2}$) was plotted as extracted from the CV curve for 0 mM and 1 mM HF (Fig. 2c) using the Dunn method[44] using eqn (2) given below.

$$\frac{i_p}{\nu^{\frac{1}{2}}} = k_1 \nu^{\frac{1}{2}} + k_2, \qquad (2)$$

where k_2 and $k_1 \nu^{1/2}$ represent the current response for diffusion-controlled contributions, and surface capacitance, respectively. The linear dependence (Fig. 2c) of peak current density with $\nu^{1/2}$ confirms the diffusion-controlled process. The k_2 values are obtained from the intercept of the ($i_p/\nu^{1/2}$) *vs.* ($\nu^{1/2}$) graph plotted with and without HF and are found to be 0.038 and 0.21 A g^{-1} V s$^{-1/2}$, respectively. In addition to HF, the increase in k_2 value indicates the dominance of diffusion-controlled contribution in the presence of HF, as indicated by the CV curve of MoO$_3$ at different concentrations (Fig. 2b).

The effect of HF on the specific capacitance was also studied to investigate it deeper, where the specific capacitance was estimated using the method mentioned in the ESI.† The variation of the specific capacitance as a function of scan rate at various concentrations of HF of MoO$_3$/GCE calculated from the CV curve was observed (Fig. S3, ESI†). A maximum specific

Table 1 Comparison of the HF electrochemical sensor with other reported sensors

S. no	Material	Sensing material	Sensitivity	LOD (μM)	Ref.
1	Bi_2Te_3	H_2O_2	4903 μA mM^{-1} cm^{-2}	0.016	15
2	Co_3O_4 $NiCo_2O_4$ NSs	H_2O_2	303.42 μA mM^{-1} cm^{-2}	0.596	17
3	Co_3O_4 $NiCo_2O_4$ NSs	Glucose	1463.13 μA mM^{-1} cm^{-2}	0.596	17
4	CoO_x NPs/cholesterol oxidase	H_2O_2	43.5 μA mM^{-1} cm^{-2}	4.2	45
5	Cu_2O on AlOOH/reduced graphene oxide	Glucose	155.1 μA mM^{-1} cm^{-2}	2.6	46
6	Fe_3O_4@Au/MnO_2	Glucose	2520 μA mM^{-1} cm^{-2}	13.2	47
7	Nanoneedle-$NiCo_2O_4$	Glucose	3000 μA mM^{-1} cm^{-2}	2	48
8	MoS_2/S-Ti_3C_2/LGE	Aristolochic acid	69.955 μA mM^{-1} cm^{-2}	—	49
9	MoS_2/S-Ti_3C_2/LGE	Roxarsone	57 μA mM^{-1} cm^{-2}	—	49
10	MoO_3	Fluorane	6656 mF mM^{-1} g^{-1}	1.5	This work

capacitance of 210 F g^{-1}, 54 F g^{-1} at 10 mV s^{-1} was calculated which decreased gradually to 95 F g^{-1}, 26 F g^{-1} at 100 mV s^{-1} for 1 mM, and 0 mM HF concentration respectively (Fig. S3, ESI†). This also indicates that the capacitance values are sensitive to the presence of HF and are affected by its concentration. To further evaluate the charging–discharging properties of MoO_3, GCD tests have been performed on MoO_3/GCE in 0.5 M $LiClO_4$ with 1 mM HF at various current densities (Fig. S4, ESI†), which also shows the variation of specific capacitance with current density (inset, Fig. S4, ESI†). A maximum specific capacitance of $\sim$110 F g^{-1} at 2 A g^{-1} was observed.

The electrochemical measurements show a variation in the specific capacitance as a function of HF concentration. A linear variation (Fig. 2d) is seen throughout the measured range and was used to calculate an HF sensitivity of $\sim$6656 mF mM^{-1} g^{-1},

which is very encouraging as compared to the values reported in the range of thousands.[45–47] In order to cross-check, the sensitivity has also been estimated by using the redox peak current as the observable quantity. A variation in peak current density with HF concentration (Fig. S5, ESI†) was used for this purpose, yielding a sensitivity of $\sim$689 μA mM^{-1} cm^{-2}. In addition to the sensitivity, the limit of detection (LOD) is also estimated from the variation of specific capacitance (or current density) with HF concentration taking the signal to noise ratio of S/N = 3. The value of 1.5 μM (or 1.2 μM) was the LOD calculated from variation of specific capacitance (or current density) with HF concentration implying a very low LOD. The almost same LOD from experiments validates the above capacitance-based experiments. The LOD and sensitivity of the fabricated HF sensor have been compared with other
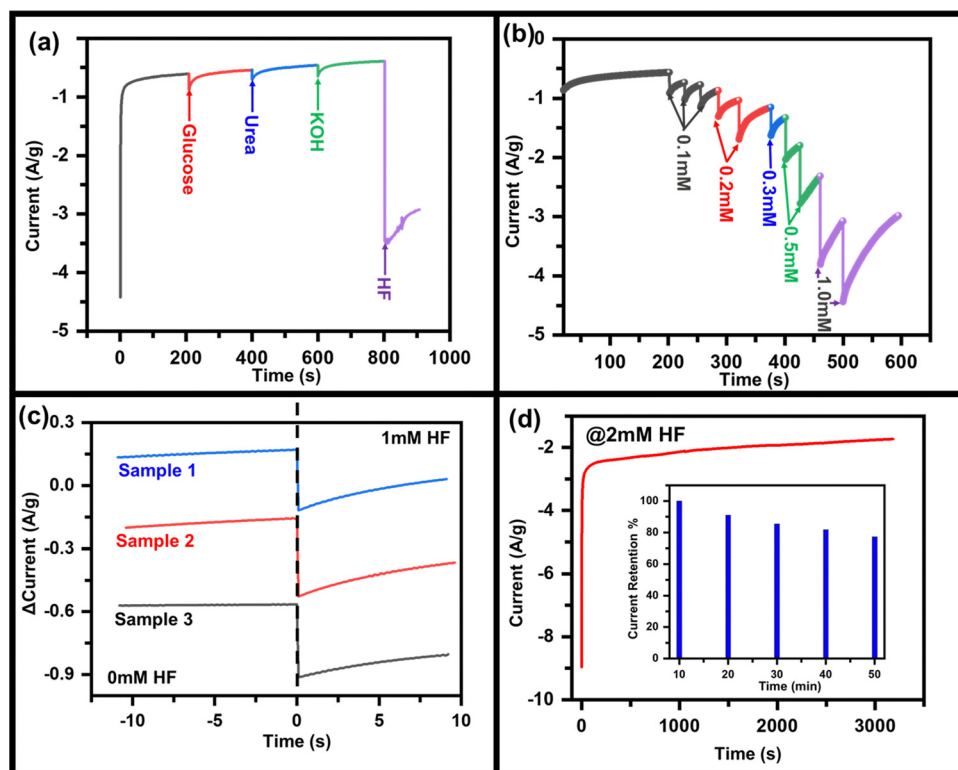

Fig. 3 Chronoamperometric response of MoO_3/CC (a) upon the addition of 1 mM HF, glucose, urea, and KOH, (b) upon the addition of different concentrations of HF (0.1, 02, 0.3, 0.5, and 1.0 mM). (c) Response time of the sensor for three different batches of the sample under 1 mM HF, and (d) long-term stability (inset: current retention *versus* time graph) test of the MoO_3/CC electrode.
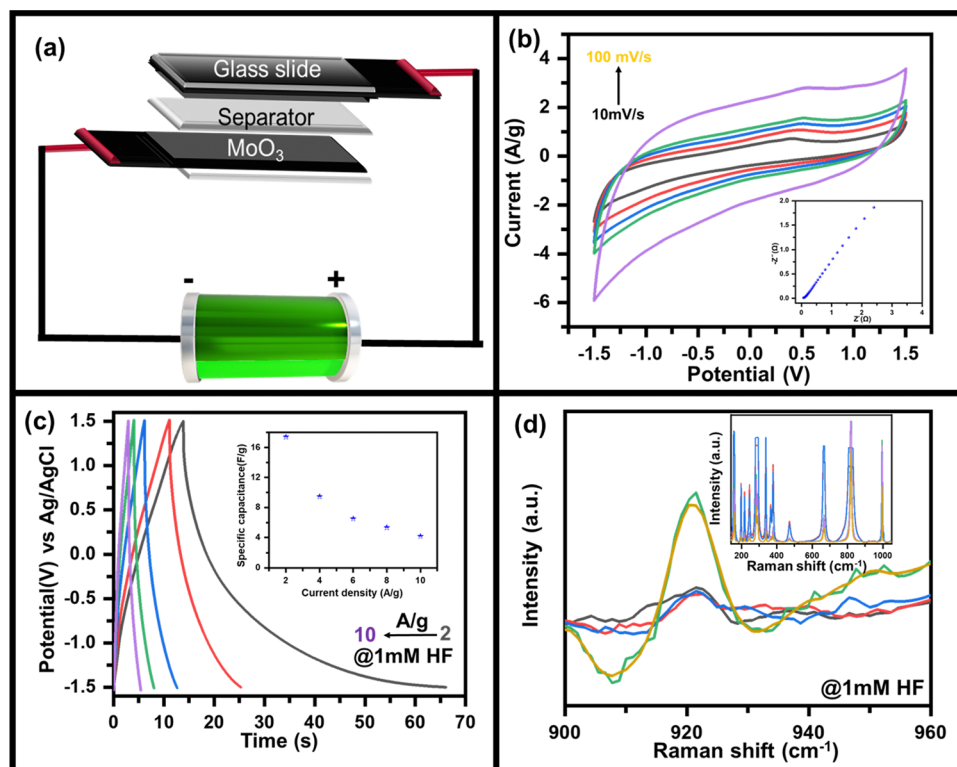
Fig. 4 (a) Schematic diagram of as-fabricated MoO_3//AC supercapacitor device, (b) CV curves measured at scan rates of 10 to 100 mV s^{-1} along with the corresponding EIS plot (ESI†), (c) GCD plots at 2 A g^{-1} to 10 A g^{-1} along with variation of specific capacitance as a function of current density (inset) and (d) *in situ* Raman spectra of asymmetric supercapacitor device during the charging and discharging process.

sensors in Table 1, indicating the superior performance of MoO_3/GCE as the HF sensor. For practical applications of a sensor, the material used in sensing must not degrade during the course of sensing so that the electrode can be used multiple times. To ensure the quality of pre- and post-sensing samples, Raman scattering was used. Fig. S6 (ESI†) indicates no change in the spectra after electrochemical measurements with (1.0 mM and 0.5 mM) and without HF in the electrolyte, confirming that the material is stable, and returns to its initial state after sensing is done.

From the above discussions, it is clear that the materials have characteristics for HF detection, but for practical applications, similar properties must be replicated on substrates that can be handled easily. To investigate the HF sensing property, MoO_3 was drop casted on the CC electrode (say MoO_3/CC) and further measurements were done. Fig. S7 (ESI†) represents the CV curve of MoO_3/CC at a 50 mV s^{-1} scan rate without HF. The CV test at 50 mV s^{-1} was performed on three identical batches of MoO_3/CC samples (Fig. S8, ESI†). No significant change in the anodic/cathodic peak current was observed, implying the MoO_3/CC has good repeatability. For an excellent electrochemical sensor, its performance should not interfere with other chemical compounds such as glucose, urea, and KOH. To show the anti-interference property of this material to the sensor, in a continuously stirred electrolytic solution, 1 mM of glucose, urea, KOH, and HF were added one after another (Fig. 3a), and the corresponding change in current was observed. With

the addition of materials other than HF, no significant change in the cathodic peak was observed. On the other hand, in addition to HF, cathodic peak current increases significantly, which also depends on the concentration of HF. Fig. 3b shows the chronoamperometry graph of MoO_3/CC at −1.3 V with various HF concentrations. A significant change in the cathodic current was observed with the continuous addition of different HF concentrations. Fig. 3c indicates a fast response time (for three different samples to check reproducibility) of the sensor, ∼2.5 s, which is generally due to mixing HF droplets in the existing electrolyte solution. Fig. 3d indicates the long-term sensing stability of the MoO_3/CC electrode under 2 mM HF at room temperature, implying that the catalyst is stable even after a continuous performance of 50 min. The sensor retains ∼80% of its maximum current after continuous working of 50 min, even at a high concentration of HF (2 mM), indicating high current stability.

As discussed above, the charge storage capability of MoO_3 has increased after HF addition in the electrolyte. Hence the suitability as the better charge storage device is tested by making an asymmetric supercapacitor device MoO_3//AC fabricated using the recipe discussed in the Experimental section as shown in the schematic (Fig. 4a). Since uniform deposition of MoO_3 on CC is essential for better electrochemical performance, it was ensured prior to using it in the device, as seen in the SEM image (Fig. S9, ESI†). In addition, enough pores could be seen in MoO_3/CC to diffuse electrolyte ions into the substrate material interface. The CV curve of the device in 0.5 M $LiClO_4$ with 1 mM HF shows a quasi-rectangular shape

(Fig. 4b), which indicates the charge storage capability of the device with an electric double-layer type charge storage mechanism. The sudden increase in current at a higher negative potential indicates the electrocatalytic properties of the device due to MoO_3.

To further confirm its charge storage capability and to understand the ion diffusion mechanism, electrochemical impedance spectroscopy was recorded at 5 mV amplitude in the frequency range 10 kHz to 10 mHz (inset: Fig. 4b). The straight line-shaped curve in the low-frequency region confirms that the device has capacitive behaviour. A small value of solution electrolyte contact resistance (as apparent from the semi-circular arc present in the high-frequency region) indicates fast charging and discharging response times. In contrast, the low value of charge transfer resistance (as seen from the radius of the semi-circular arc in the high-frequency region) indicates that the MoO_3//AC is an efficient device for the diffusion and charge transfer of electrolyte ions. Furthermore, the galvanostatic charging discharging (GCD) profile of the MoO_3//AC device was recorded at 2 A g^{-1} to 10 A g^{-1} current density (Fig. 4c) to determine the charge storage capability of the device by measuring the specific capacity (inset, Fig. 4c). The GCD plot of the device indicates a high Coulombic efficiency indicating the suitability of the device for practical use. The non-linear discharging profile in the negative potential indicates the redox activity of MoO_3, whereas the linear discharging in the positive region indicates the activity of AC. The asymmetric MoO_3//AC supercapacitive device shows a capacitance of ~ 17 F g^{-1} at 2 A g^{-1}, decreasing to ~ 4 F g^{-1} at 10 A g^{-1} (inset, Fig. 4c) as calculated using eqn S2 (ESI†).

In situ Raman spectroscopy was done to further understand the mechanism of the charge storage process and HF sensitivity in MoO_3 due to its advantage in probing fine characteristics of nanomaterials.[50–52] Raman spectra were recorded while the device was applied when the device was under charging conditions (applied bias of -1.5 V). A similar Raman spectrum was recorded when the device was discharged (unbiased state). The Raman spectra (inset, Fig. 4d) in the charging state show an additional peak at ~ 920 cm^{-1} which was absent when the device was unbiased (as-prepared), as can be clearly seen in the zoomed in portion of the Raman spectrum (Fig. 4d). The peak at ~ 920 cm^{-1} was assigned to be originating from the reduced state of MoO_3 (*i.e.*, MoO_2),[53,54] where Mo is present in the +IV state against the +VI state in the as-deposited form. Overall, the MoO_3 shows excellent electro-reduction of HF under neutral conditions and can be used as sensing. This can also be used for supercapacitive energy storage applications, as demonstrated by making a solid-state supercapacitor, where charge storage capabilities come from the bias-induced redox activity of MoO_3 as validated using *in situ* Raman spectroscopy.

Conclusions

Electrochemical measurements from microcrystalline MoO_3, prepared using a simple sol–gel method, reveal that it can be used in bifunctional applications in energy storage and HF

detection. The MoO_3 shows pseudocapacitance behavior with a specific capacitance of 210 F g^{-1} (at 10 mV s^{-1}) with a linear increase in the specific capacitance value and electroreduction current peak with HF concentration. The linear variation of specific capacitance with HF concentration reveals a sensitivity value as high as 6656 mF mM^{-1} g^{-1} and a LOD value as low as 1.2 µM at an S/N ratio of 3. The chronoamperometric response of MoO_3 reveals the high selectivity of HF sensing as well as the HF concentration with more than 80% current retention after continuous use of 3000 s at very maximum sensing concentration of 2 mM of HF with excellent electrode stability as revealed using Raman spectroscopy. The charge storage properties can be utilized for energy storage applications, as demonstrated by measuring the supercapacitor measurements from a solid-state prototype device. In the presence of HF, the target ions reduce Mo(+VI) to Mo(+VIII), as confirmed using *in situ* Raman spectroscopy carried out during the charging and discharging process of the capacitor.

Conflicts of interest

There are no conflicts to declare.

Acknowledgements

References

1 Ç. K. Dindar, Md. Z. Kabir and B. Uslu, *Recent Developments in Green Electrochemical Sensors: Design, Performance, and Applications*, American Chemical Society, 2023, vol. 1437, pp. 307–340.

2 H.-Y. Chou, J.-L. Chiang, C.-T. R. Yu, J.-M. M. Chen and D.-S. Wuu, *Sens. Actuators, A*, 2023, **349**, 114071.

3 B. G. Loganathan, S. Ahuja and B. Subedi, *Contaminants in Our Water: Identification and Remediation Methods*, American Chemical Society, 2020, vol. 1352, pp. 13–39.

4 S. Qiao, A. Sampaolo, P. Patimisco, V. Spagnolo and Y. Ma, *Photoacoustics*, 2022, **27**, 100381.

5 T. Liang, S. Qiao, X. Liu and Y. Ma, *Chemosensors*, 2023, **11**, 41.

6 R. C. Ropp, in *Encyclopedia of the Alkaline Earth Compounds*, ed. R. C. Ropp, Elsevier, Amsterdam, 2013, pp. 25–104.

7 S. E. Gad, in *Encyclopedia of Toxicology*, ed. P. Wexler, Elsevier, New York, 2nd edn, 2005, pp. 542–543.

8 X. Liu, S. Qiao, G. Han, J. Liang and Y. Ma, *Photoacoustics*, 2022, **28**, 100422.

9 B. Monteiro, J. P. Leal, M. Outis, M. H. Casimiro and C. C. L. Pereira, *J. Mater. Chem. C*, 2023, **11**, 5199–5207.

10 J. Wang, P. Hui, X. Zhang, X. Cai, J. Lian, X. Liu, X. Lu and W. Chen, *Anal. Chem.*, 2022, **94**, 17240–17247.

11 L. Mu, W. Shi, J. C. Chang and S.-T. Lee, *Nano Lett.*, 2008, **8**, 104–109.

12 J. H. Lee, M. S. Park, H. Jung, Y.-S. Choe, W. Kim, Y. G. Song, C.-Y. Kang, H.-S. Lee and W. Lee, *Sens. Actuators, B*, 2020, **307**, 127598.

13 G. Liu, M. Lu, X. Huang, T. Li and D. Xu, *Sensors*, 2018, **18**, 4166.

14 F. Yang, G. Jiang, F. Yan and Q. Chang, *Microchim. Acta*, 2019, **186**, 417.

15 F. Zhao, S. Zhou and Y. Zhang, *ACS Appl. Mater. Interfaces*, 2021, **13**, 4761–4767.

16 S. Mishra, P. Yogi, P. R. Sagdeo and R. Kumar, *Nanoscale Res. Lett.*, 2018, **13**, 1–7.

17 D. Chen, D. Pang, S. Zhang, H. Song, W. Zhu and J. Zhu, *Electrochim. Acta*, 2020, **330**, 135326.

18 S. Mishra, P. Yogi, P. R. Sagdeo and R. Kumar, *ACS Appl. Energy Mater.*, 2018, **1**, 790–798.

19 T. Ghosh, C. Rani, S. Kandpal, M. Tanwar, L. Bansal and R. Kumar, *J. Phys. D: Appl. Phys.*, 2022, **55**, 365103.

20 F. Wang, J. Jia, W. Zhao, L. Zhang, H. Ma, N. Li and Y. Chen, *Mater. Sci. Semicond. Process.*, 2022, **151**, 106986.

21 R. Zakaria, M. Mahbub and C. S. Lim, *Results in Optics*, 2023, **11**, 100374.

22 A. S. Agnihotri, A. Varghese and M. Nidhin, *Appl. Surf. Sci. Adv.*, 2021, **4**, 100072.

23 S. Kandpal, T. Ghosh, C. Rani, A. Chaudhary, J. Park, P. S. Lee and R. Kumar, *ACS Energy Lett.*, 2023, 1870–1886.

24 T. Ghosh, S. Kandpal, C. Rani, A. Chaudhary and R. Kumar, *Adv. Opt. Mater.*, 2023, **11**, 2203126.

25 B. B. Sahoo, V. S. Pandey, A. S. Dogonchi, P. K. Mohapatra, D. N. Thatoi, N. Nayak and M. K. Nayak, *J. Energy Storage*, 2023, **65**, 107335.

26 T. Ghosh, L. Bansal, S. Kandpal, C. Rani, D. K. Rath, B. Sahu, S. Chhoker and R. Kumar, *J. Energy Storage*, 2023, **72**, 108640.

27 S. Kandpal, L. Bansal, A. Ghanghass, T. Ghosh, C. Rani, B. Sahu, D. K. Rath, R. Bhatia, S. Ivaturi and R. Kumar, *J. Mater. Chem. C*, 2023, DOI: **10.1039/D3TC01880F**.

28 Q. Song, S. Zhou, S. Wang, S. Li, L. Xu and J. Qiu, *Chem. Eng. J.*, 2023, **461**, 142033.

29 L. Bansal, C. Rani, T. Ghosh, S. Kandpal, M. Tanwar and R. Kumar, *Silicon*, 2023, **15**, 167–175.

30 T. Ghosh, L. Bansal, S. Kandpal, C. Rani, M. Tanwar and R. Kumar, *ACS Appl. Opt. Mater.*, 2023, **1**, 473–480.

31 T. Ghosh, S. Kandpal, C. Rani, L. Bansal, M. Tanwar and R. Kumar, *Adv. Electronic Mater.*, 2023, **9**, 2201042.

32 I. Shakir, M. Shahid, H. W. Yang and D. J. Kang, *Electrochim. Acta*, 2010, **56**, 376–380.

33 D. Li, Y. Li, F. Li, J. Zhang, X. Zhu, S. Wen and S. Ruan, *Ceram. Int.*, 2015, **41**, 4348–4353.

34 P. Thomas, C. W. Lai and M. R. Johan, *Chemosphere*, 2022, **308**, 136214.

35 S. Z. Noby, A. Mohanty, P. Zirak, A. Ramadoss and L. Schmidt-Mende, *J. Alloys Compd.*, 2022, **918**, 165530.

36 L. Cao, J. He, J. Li, J. Yan, J. Huang, Y. Qi and L. Feng, *J. Power Sources*, 2018, **392**, 87–93.

37 A. E. Elkholy, T. T. Duignan, R. Knibbe and X. S. Zhao, *Electrochim. Acta*, 2022, **429**, 141050.

38 B. N. Rashmi, S. F. Harlapur, C. R. Ravikumar, B. Avinash, K. Gurushantha, M. B. Divakara, M. S. Santosh and K. Veena, *Mater. Today: Proc.*, 2021, **46**, 5931–5935.

39 L. Zhang, X. Yang, F. Zhang, G. Long, T. Zhang, K. Leng, Y. Zhang, Y. Huang, Y. Ma, M. Zhang and Y. Chen, *J. Am. Chem. Soc.*, 2013, **135**, 5921–5929.

40 L. O. Alemán-Vázquez, E. Torres-García, J. R. Villagómez-Ibarra and J. L. Cano-Domínguez, *Catal. Lett.*, 2005, **100**, 219–226.

41 M. Yoonessi, A. Borenstein, M. F. El-Kady, C. L. Turner, H. Wang, A. Z. Stieg and L. Pilon, *ACS Appl. Energy Mater.*, 2019, **2**, 4629–4639.

42 S. K. Sen, U. C. Barman, M. S. Manir, P. Mondal, S. Dutta, M. Paul, M. A. M. Chowdhury and M. A. Hakim, *Adv. Nat. Sci.: Nanosci. Nanotechnol.*, 2020, **11**, 025004.

43 N. G. Prakash, M. Dhananjaya, A. L. Narayana, H. Maseed, V. V. S. S. Srikanth and O. M. Hussain, *Appl. Phys. A: Mater. Sci. Process.*, 2019, **125**, 488.

44 J. Wang, J. Polleux, J. Lim and B. Dunn, *J. Phys. Chem. C*, 2007, **111**, 14925–14931.

45 A. Salimi, R. Hallaj and S. Soltanian, *Electroanalysis*, 2009, **21**, 2693–2700.

46 Z. Yang, X. Yan, Z. Li, X. Zheng and J. Zheng, *Anal. Methods*, 2016, **8**, 1527–1531.

47 A. Samphao, P. Butmee, J. Jitcharoen, Ľ. Švorc, G. Raber and K. Kalcher, *Talanta*, 2015, **142**, 35–42.

48 D. K. Pathak, A. Chaudhary, M. Tanwar, U. K. Goutam, P. Mondal and R. Kumar, *ACS Appl. Nano Mater.*, 2021, **4**, 2143–2152.

49 U. Rajaji, P.-S. Ganesh, S.-Y. Kim, M. Govindasamy, R. A. Alshgari and T.-Y. Liu, *ACS Appl. Nano Mater.*, 2022, **5**, 3252–3264.

50 C. Rani, M. Tanwar, T. Ghosh, S. Kandpal, D. K. Pathak, A. Chaudhary, P. Yogi, S. K. Saxena and R. Kumar, *Anal. Chem.*, 2022, **94**, 1510–1514.

51 M. Tanwar, L. Bansal, C. Rani, S. Rani, S. Kandpal, T. Ghosh, D. K. Pathak, I. Sameera, R. Bhatia and R. Kumar, *ACS Phys. Chem Au*, 2022, **2**, 417–422.

52 C. Rani, S. Kandpal, T. Ghosh, L. Bansal, M. Tanwar and R. Kumar, *Phys. Chem. Chem. Phys.*, 2023, **25**, 1627–1631.

53 O. F. Oyerinde, C. L. Weeks, A. D. Anbar and T. G. Spiro, *Inorg. Chim. Acta*, 2008, **361**, 1000–1007.

54 L. J. Willis, T. M. Loehr, K. F. Miller, A. E. Bruce and E. I. Stiefel, *Inorg. Chem.*, 1986, **25**, 4289–4293.